Two-Dimensional Mechanism of Hovering Flight by Single Flapping Wing

Dokyun Kim, Haecheon Choi*

School of Mechanical and Aerospace Engineering, Seoul National University, Seoul 151-744, Korea

Numerical simulations are conducted to investigate the mechanism of hovering flight with an inclined stroke. The Reynolds numbers considered are 150 and 1000 based on the maximum translational velocity and wing chord length. Three mechanisms responsible for high vertical force generation, suggested by Dickinson et al. (1999), are confirmed and more elaborated in the present study. First, we show that the vertical force during downstroke is larger than that from the quasi-steady analysis due to the delayed stall mechanism. Second, the wing-wake interaction of reducing the negative vertical force during the stroke reversal is explained in terms of the reattachment of the vortex, shed previously during downstroke, on the wing, by which the wing is submerged in a low pressure region during upstroke and has a smaller negative vertical force. Finally, the rotational circulation is explained by advancing the rotation timing of the wing at supination using both the numerical simulation and inviscid potential theory.

Key Words : Insect Flight, CFD, Lift Force, Vortex Interaction, Circulation

Nomenclature

a : Major axis of the ellipse
A_m : Stroke amplitude
b : Minor axis of the ellipse
c : Chord length of the wing
C_D : Drag coefficient
C_H : Horizontal force coefficient
C_L : Lift coefficient
C_{rot} : Hydrodynamic lift force coefficient due to wing rotation
C_V : Vertical force coefficient
C_{Va} : Vertical force coefficient due to added mass
C_{Vqs} : Vertical force coefficient with the quasi-steady assumption
f : Wing beat frequency
g : Gravity acceleration
h : Thickness of the wing
l : Wing span
p : Pressure
Re : Reynolds number, $Re=u_{\max}c/\nu$
t : Time
T : Period of the flapping motion
$\mathbf{u}_d, u_d$: Translational velocity of the wing
$u_{\max}$: Maximum translational velocity during flapping
$\mathbf{x}'$: Position vector in a moving reference frame, (x', y')
(x_c, y_c) : Position of the wing center
α : Angle between the chord axis and the stroke plane
α_d : Constant value of α during the downstroke period
$\tilde{\alpha}_d$: Optimal α_d for maximum vertical force
α_u : Constant value of α during the upstroke period
β : Angle of the stroke plane to the horizontal axis
ν : Kinematic viscosity
ρ : Fluid density
$\boldsymbol{\Omega}, \Omega$: Angular velocity of the wing

* Corresponding Author,
E-mail : choi@snu.ac.kr
TEL : +82-2-880-8361; **FAX** : +82-2-878-3662
School of Mechanical and Aerospace Engineering, Seoul National University, Seoul 151-744, Korea. (Manuscript **Received** July 7, 2006; **Revised** October 23, 2006)

1. Introduction

The insect-flight mechanism is important in biomechanics due to its direct applicability to the design of micro air vehicles. The first advance in the theory of insect flight was made by Weis-Fogh and Jenson (1956), who introduced a quasi-steady analysis. The quasi-steady analysis is such that the instantaneous force on the flapping wing is calculated from the steady state condition. However, Ellington (1984a) showed that the quasi-steady analysis fails to explain high lift generated by the hovering motion of some insects. Hovering flight is an ideal case for investigation of unsteady mechanism since it is the extreme condition where the flight velocity is zero. Therefore, unsteady mechanisms, which may explain such high lift, have been investigated by many researchers over the past two decades in the case of hovering flight.

One of the most important unsteady mechanisms is associated with the generation of a leading-edge vortex, called delayed stall : i.e., when a wing starts impulsively from rest at an angle of attack larger than the stall angle, a large vortical structure is generated at the leading edge of the wing, and this intense leading-edge vortex increases lift until it sheds from the wing (Francis and Cohen, 1933). This mechanism was first verified by Walker (1931) for the model aircraft wing at a high angle of attack. However, the lift enhancement by the delayed stall did not persist after a few chord lengths of travel and lift dropped as the leading-edge vortex shed.

On the other hand, recent experiments about insect flights showed that the leading-edge vortex does not shed even after several chord lengths of travel. Ellington et al.(1996) visualized the flow around a flapping wing using a hawkmoth flapper model and observed an intense leading edge vortex during the whole downstroke period. They suggested that this leading edge vortex is stabilized by the spanwise helical flow existing along the wing axis and thus lift is enhanced by sustaining the attachment of the leading-edge vortex on the wing. This new three-dimensional mechanism was numerically confirmed by Liu et al.(1998). However, this spanwise helical flow was not observed in a fruitfly flapping model (Birch and Dickinson, 2001). The corresponding Reynolds number of the fruitfly model is much lower than that of the hawkmoth model (Ellington et al., 1996). Therefore, the three-dimensional mechanism (the stabilization of the leading-vortex by the spanwise helical flow) may not be applicable to insect flights at low Reynolds numbers.

Recently, Dickinson et al.(1999) proposed three mechanisms from the experiment of the model wing of a Drosophila : delayed stall, rotational circulation, and 'wake capture'. While the delayed stall occurs during the translational phase of the wing motion, two other mechanisms are related to the stroke reversal of wing. They measured forces on the wing and found that double peaks occurred during the stroke reversal. The first peak occurred while the wing was rotating, and they suggested that the wing rotation itself serves as a source of circulation to enhance the lift force. This mechanism, called rotational circulation, is similar to the Magnus effect because the sign of this peak is determined by the timing of wing rotation. The second peak occurred right after the wing rotation, and they concluded that this peak occurs due to the interaction between the wing and vortex shed previously. This wing-wake interaction was called 'wake capture' in Dickinson et al.(1999). However, the detailed feature of this 'wake capture' was not given in that study due to the complexity of flow around the wing during the stroke reversal.

Sun and Tang (2002) conducted a three-dimensional numerical simulation of flow from the wing motion of a fruitfly whose kinematics is similar to that in Dickinson et al.(1999). They concluded that wake from the previous stroke reduced lift because it generated downwash velocity in front of wing. Therefore, they did not accept the idea of lift enhancement by wing-wake interaction. Instead, it was suggested that rapid acceleration of wing at the beginning of wing stroke is the main reason for the force peak during the stroke reversal. At present, this controversy has not been resolved.

Although the real insect flight is fully three-

dimensional, recent two-dimensional numerical simulations show interesting and useful results. Wang (2000) investigated the hovering motion of a dragonfly by two-dimensional numerical simulation and showed that a sufficient vertical force can be generated by a two-dimensional figure-eight wing motion to stay aloft. Wang et al. (2004) showed that there is no noticeable discrepancy in force generation between the two-dimensional computation and three-dimensional experiment. These two numerical results suggest that three-dimensional simulations are not necessarily required to explain high lift generated during hovering motion. Therefore, two-dimensional simulation is an appropriate and effective tool to investigate unsteady mechanisms for high lift generation.

In contrast to most insects hovering with a horizontal stroke, some insects such as dragonflies hover with an inclined stoke. The inclined stroke has a disadvantage for the generation of the vertical force (in the opposite direction to that of the gravitational acceleration), because a negative one is generated during the upstroke. However, dragonflies have fascinated scientists because of their great aerodynamic performance and maneuverability. Therefore, it is interesting to study how dragonflies can generate such high vertical force in spite of an inclined stroke. Fig. 1 shows three different wing motions according to the force-generating mechanism. For hovering with a horizontal stroke, sometimes called normal hovering, vertical forces are provided by lift alone, whereas for hovering with a vertical stroke, called rowing, they are generated only by drag (Vogel, 1994). Flapping with an inclined stroke may be considered as a combination of horizontal and vertical strokes, and both drag and lift contribute to the vertical force in this case.

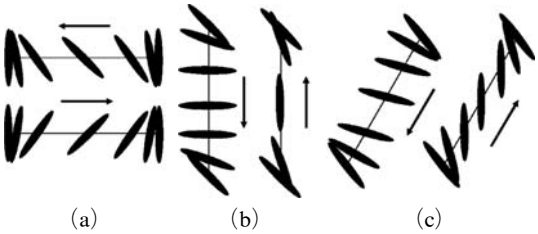

Fig. 1 Three different wing motions according to the force-generating mode: (a) normal hovering with a horizontal stroke; (b) rowing with a vertical stroke; (c) hovering with an inclined stroke

So far, nearly no research has been performed on the hovering with an inclined stroke as compared to a horizontal stroke. Wang (2000) conducted two-dimensional numerical simulation for hovering motion of a dragonfly and observed that the vortices shed from the leading and trailing edges of the wing form a vertical-force-generating vortex dipole when the wing rotates at the end of downstroke motion. She suggested that this vortex dipole generation is a crucial unsteady mechanism for the hovering motion of a dragonfly. However, this explanation is not sufficient to explain high lift generation by the inclined stroke, and other unsteady mechanisms should be searched for and examined further.

Therefore, the objective of the present study is to numerically investigate the unsteady mechanisms of the hovering with an inclined stroke. We examine in detail three unsteady mechanisms, originally conjectured by Dickinson et al. (1999): delayed stall, wing-wake interaction and rotational circulation. In this study, we provide a new explanation for the wing-wake interaction from the temporal evolution of vortical structures around the wing. The effects of wing acceleration and rotation are also studied by using the concept of added mass and circulation theorem, respectively. The wing shape considered in the present study is a two-dimensional elliptic wing (Wang, 2000). The Reynolds numbers investigated are $Re=150$ and 1000 based on the maximum translational velocity during flapping and the chord length of the wing. These Reynolds numbers correspond to the flapping motions by the fruitfly and dragonfly, respectively (Birch and Dickinson 2001; Wakeling and Ellington 1997).

2. Numerical Details

Figure 2 shows the flapping motion with an inclined stroke and the force definition on the wing. Following Wang (2000), the position of the

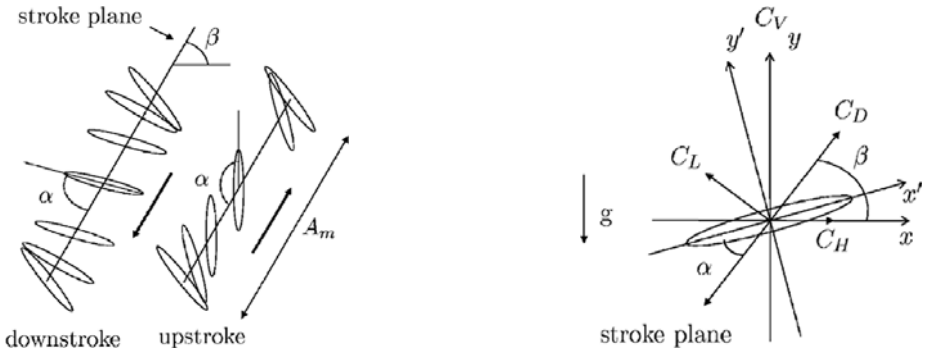

Fig. 2 (a) Flapping motion of the wing; (b) definition of the forces during downstroke

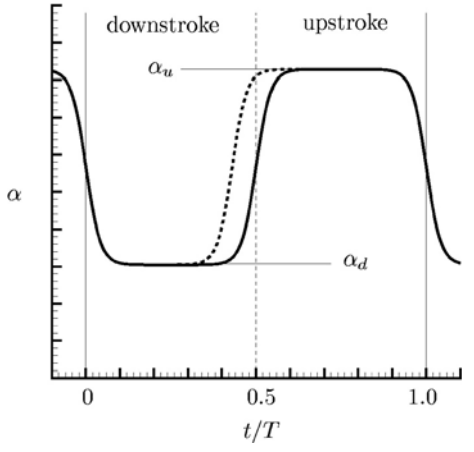

Fig. 3 Variation of α in time: ——, symmetric rotation (t_s=0); ----, early rotation (t_s<0). Here T is the period of flapping motion

wing center (x_c, y_c) is given by

$$x_c=0.5A_m\cos(2\pi ft)\cos\beta$$
$$y_c=0.5A_m\cos(2\pi ft)\sin\beta \qquad (1)$$

where A_m=2.5c. C_H and C_V denote the horizontal and vertical force coefficients, and C_L and C_D are the lift and drag coefficients, respectively (see Fig. 2(b)). The thickness-to-chord ratio of the wing is h/c=0.125 following Wang (2000).

Figure 3 shows the time variation of angle α, For flapping flight, the wing rapidly rotates and changes its direction during the stroke reversal. The counter-clockwise rotation of the wing at the end of upstroke is called pronation and the clockwise one at the end of downstroke is called supination. For real insects, pronation and supination are approximately equal in duration, and each action period is relatively short compared with the translation period (Ellington, 1984b). In order to represent these characteristics, we model $\alpha(t)$ in the following manner:

$$\alpha(t)=\begin{cases}\xi\tanh(-\delta t)+\gamma, & -\frac{T}{4}\le t<\frac{T}{4}\\ \xi\tanh\left[\delta\left(t-\frac{T}{2}-t_s\right)\right]+\gamma, & \frac{T}{4}\le t<\frac{3}{4}T\end{cases} \qquad (2)$$

Here, T is the period of flapping motion, $\xi=(\alpha_u-\alpha_d)/2$, $\gamma=(\alpha_u+\alpha_d)/2$, and α_d and α_u are the constant values of α during the downstroke and upstroke translation periods, respectively, as shown in Fig. 3. δ is a parameter determining the rotation period and is chosen to be δ=2 for most simulations conducted in this study. At δ=2, the rotation period occupies about 30% of the total flapping period. t_s is a parameter adjusting the timing of rotation at supination. For t_s=0, the pronation and supination occur symmetrically, but the supination occurs earlier for t_s<0. Unless otherwise specified, t_s=0 in this paper.

In order to simulate the flow around a flapping wing, the Navier-Stokes and continuity equations are transformed in a fully conservative form in a non-inertial reference frame fixed to a wing body (Beddhu et al., 1996; Kim and Choi, 2006). Also, an immersed boundary method developed by Kim et al.(2001) and Kim and Choi (2006) is used to satisfy the no-slip condition on the wing surface in a Cartesian coordinate system by providing momentum forcing and mass source/sink, respectively, into the Navier-Stokes and continuity equa-

tions. Then, the governing equations become

$$\left(\frac{\partial \mathbf{u}}{\partial t}\right)_r+\nabla\cdot[(\mathbf{u}-\mathbf{v})\mathbf{u}+\mathbf{u}\mathbf{w}] =-\nabla p+\frac{1}{Re}\nabla^2\mathbf{u}+\mathbf{f} \tag{3}$$

$$\nabla\cdot\mathbf{u}-q=0 \tag{4}$$

where $\mathbf{u}=\mathbf{u}_r+\mathbf{v}$, $\mathbf{v}=\boldsymbol{\Omega}\times\mathbf{x}'+\mathbf{R}^T\mathbf{u}_d$, and $\mathbf{w}=\boldsymbol{\Omega}\times\mathbf{x}'$. As for the immersed boundary method (Kim and Choi, 2006; Kim et al., 2001), $\mathbf{f}$ is the momentum forcing vector defined at the cell faces like the velocity vector, and q is the mass source/sink defined at the cell center. The momentum forcing and mass source/sink are zero outside the body. The details about how to determine $\mathbf{f}$ and q are described in detail in Kim et al.(2001) and Kim and Choi (2006). The time integration for Eqs. (3) and (4) is based on a fractional-step method and we use a second-order semi-implicit time advancement scheme consisting of a third-order Runge-Kutta method for the convection terms and the Crank-Nicolson method for the diffusion terms. The second-order central difference scheme is used for all the spatial derivative terms in a staggered grid system. All the variables are non-dimensionalized by the maximum translational velocity $u_{\max}$ during flapping and the chord length of the wing c. The cross-section of the wing adopted in the present study is an ellipse with a thickness-to-chord ratio of 0.125 according to the model suggested by Wang (2000). Two Reynolds numbers of $Re=100$ and 1000 are considered in this study.

The size of the computational domain used is $-20c<x'<20c$ and $-20c<y'<20c$. The convective boundary conditions (Pauley et al., 1990) are used for all outer boundaries. Non-uniform meshes are used with dense grid clustering around the wing for accurately resolving the vortical motion there. The numbers of grid points are 370×416 in x' and y' directions, respectively. Fig. 4 shows the mesh near the wing, where 50×25 grid points are uniformly distributed inside the wing.

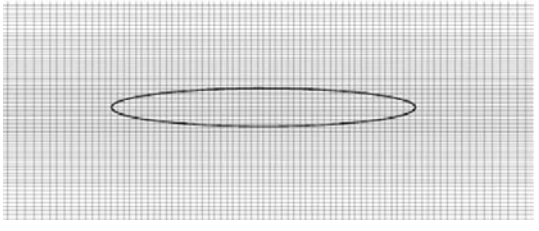

Fig. 4 Mesh near the wing

First, we simulate the same flow considered in Wang (2000), flow around a hovering wing with an inclined stroke. The cross-section and center position of the wing are the same as above. Following Wang (2000), the angle of attack is defined as

$$\alpha'(t)=\frac{\pi}{4}-\frac{\pi}{4}\sin\left(\frac{2\pi t}{T}\right) \tag{5}$$

where $\alpha'=\alpha-\beta$ (Fig. 2). The values of the kinematic parameters considered by Wang (2000) are $A_m=2.5c$ and $\beta=60°$, and the simulation is carried out at $Re=157$.

Figure 5 shows the time sequence of the spanwise vorticity at $Re=157$. As shown in this figure, the rotation of the wing combines vortices

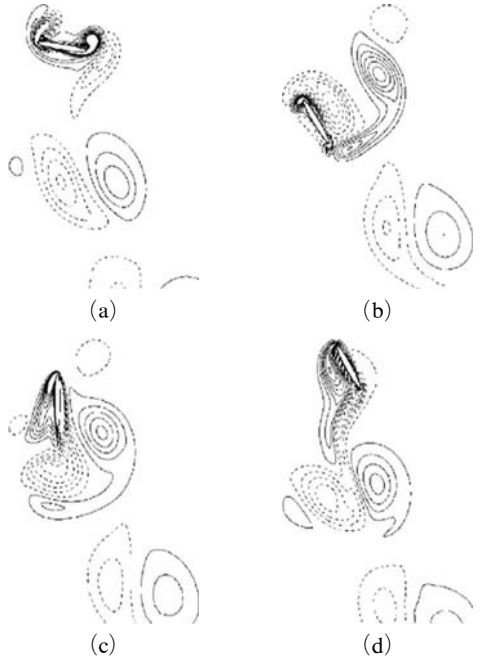

Fig. 5 Time sequence of the spanwise vorticity for $\beta=60°$ at $Re=157$: (a) $t/T=0.25$; (b) 0.45; (c) 0.75; (d) 0.95. The vorticity contour levels are $w_z c/u_{\max}=-8\sim 8$ by increments of 0.8. Negative values are dashed

shed from the leading and trailing edges of the wing as observed in Wang (2000). The vortical evolution shown in Fig. 5 is essentially the same as that in Wang (2000). Fig. 6 shows the time historis of forces on the wing, together with those by Wang (2000). In general, the present result agrees well with that by Wang (2000). However, there is a certain difference between two solutions in the beginning of the downstroke and upstroke. We doubled the grid points and the computational domain size, respectively, but the same results as shown in Fig. 6 were obtained. The reason for such a difference is unclear at present. Our numerical method and computer code have been tested for various flow problems (Kim and Choi, 2006).

3. Results

In this section, we investigate three mechanisms responsible for high vertical force, originally conjected by Dickinson et al.(1999), during hovering motion : delayed stall, wing–wake interaction and rotational circulation.

3.1 Delayed stall

As mentioned previously, delayed stall occurs when a wing starts impulsively from rest at an

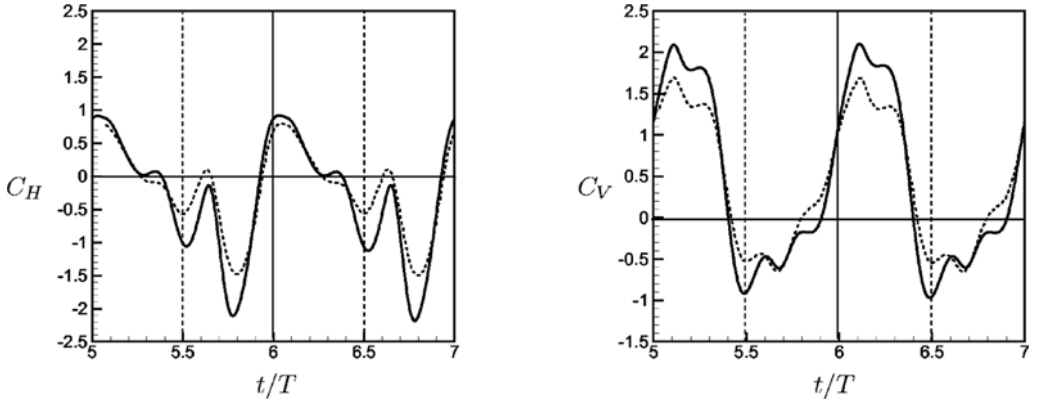

Fig. 6 Time histories of the force coefficients at $Re=157$: (a) C_H ; (b) C_V. ——, Present study ; ----, Wang (2000)

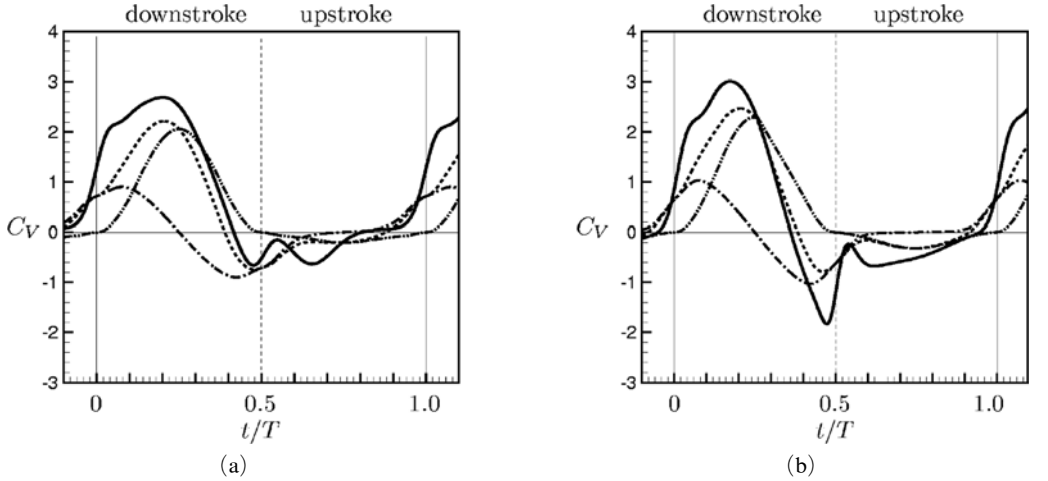

Fig. 7 Time histories of the vertical force coefficients at $Re=150$: (a) $\beta=60°$ ($\alpha_d=75°$ and $\alpha_u=150°$): (b) $\beta=90°$ ($\alpha_d=90°$ and $\alpha_u=180°$). ——, C_V ; -·-·-·-·-, C_{Vqs} ; -·-·-·-, C_{Va} ; ----, $C_{Vqs}+C_{Va}$

angel of attack larger than a stall angle. Then a large vortex forms at the leading edge of the wing and increases drag and lift. Therefore, the quasi-steady analysis (Ellington, 1984a) cannot explain the high lift during flapping motion. Fig. 7 shows the time histories of the vertical force for the cases of $\beta=60°$ and 90°, together with the quasi-steady vertical force ($F_{Vqs}=C_{Vqs}\cdot 1/2\rho u_{\max}^2 cl$), force due to added mass ($F_{Va}=C_{Va}\cdot 1/2\rho u_{\max}^2 cl$) and their sum. Here, C_{Vqs} is obtained as follows : Given the translational velocity u_d and angle α of the wing at each time t, we conduct an unsteady numerical simulation and obtain the time-averaged drag and lift forces on the wing, $F_{Dqs}(t)$ and $F_{Lqs}(t)$, respectively. Then, the quasi-steady vertical force coefficient C_{Vqs} becomes

$$C_{Vqs}(t)=\frac{F_{Vqs}}{\frac{1}{2}\rho u_{\max}^2 cl}=\frac{u_d^2(t)}{u_{\max}^2}\frac{F_{Dqs}(t)}{\frac{1}{2}\rho u_d^2(t)\,cl}\sin\beta+\frac{u_d^2(t)}{u_{\max}^2}\frac{F_{Lqs}(t)}{\frac{1}{2}\rho u_d^2(t)\,cl}\cos\beta \tag{6}$$

The force due to added mass, which is the hydrodynamic force due to the acceleration of the wing, can be obtained by (Newman, 1986)

$$F_{ah}=-\frac{\mathrm{d}u_{dx}}{\mathrm{d}t}m_{11}-\frac{\mathrm{d}u_{dy}}{\mathrm{d}t}m_{12}+u_{dx}\Omega m_{21}+u_{dy}\Omega m_{22} \tag{7}$$

$$F_{av}=-\frac{\mathrm{d}u_{dx}}{\mathrm{d}t}m_{21}-\frac{\mathrm{d}u_{dy}}{\mathrm{d}t}m_{22}-u_{dx}\Omega m_{11}-u_{dy}\Omega m_{12} \tag{8}$$

where $u_{dx}=u_d\cos\beta$ and $u_{dy}=u_d\sin\beta$. The added mass tensor $[m]$ for an ellipse with major and minor axes of a and b, respectively, in the moving reference frame (x', y') is (Newman, 1986)

$$m'_{11}=\pi\rho b^2 \tag{9}$$

$$m'_{22}=\pi\rho a^2 \tag{10}$$

$$m'_{12}=m'_{21}=0 \tag{11}$$

When the ellipse is inclined at an angle $\alpha-\beta$ from the x-axis, the added mass tensor is $[m]=R^{-1}(\alpha-\beta)[m']R(\alpha-\beta)$ where R is the rotational matrix. Then, the added mass tensor in the (x, y) coordinates becomes

$$m_{11}=\pi\rho b^2\cos^2(\alpha-\beta)+\pi\rho a^2\sin^2(\alpha-\beta) \tag{12}$$

$$m_{22}=\pi\rho b^2\sin^2(\alpha-\beta)+\pi\rho a^2\cos^2(\alpha-\beta) \tag{13}$$

$$m_{12}=m_{21}=-\pi\rho b^2\sin(\alpha-\beta)\cos(\alpha-\beta)+\pi\rho a^2\sin(\alpha-\beta)\cos(\alpha-\beta) \tag{14}$$

The vertical force coefficient due to added mass becomes

$$C_{Va}=\frac{F_{av}}{\frac{1}{2}\rho u_{\max}^2 cl} \tag{15}$$

where F_{av} is obtained from Eqs. (8), (12), (13) and (14).

It is clearly shown in Fig. 7 that during the translation period of downstroke, the force coefficient from the quasi-steady assumption (C_{Vqs}) is quite different from that obtained from unsteady simulation (C_V). However, when the quasi-steady force coefficient is added by the added-mass force coefficient, it ($C_{Vqs}+C_{Va}$) becomes much closer to C_V but still is smaller during most downstroke period than, supporting the conclusion of Ellington (1984a). On the other hand, the negative C_V near the end of the downstroke is larger than $C_{Vqs}+C_{Va}$ for $\beta=90°$ (Fig. 7(b)) and the negative C_V at the initial period of upstroke is smaller than $C_{Vqs}+C_{Va}$ for $\beta=60°$ (Fig. 7(a)). Therefore, it is clear that the behavior of the vertical force during the stroke reversal cannot be explained by the delayed stall mechanism.

Since the mechanism of delayed stall is closely associated with the angle of attack during the downstroke motion, it should be interesting to search for an optimal angle of attack ($\tilde{\alpha}_d$) at which the vertical force becomes maximum at a given stroke plane angle, and also to find a simple relation between the optimal angle of attack and the stroke plane angle. Hence, we investigate the effect of α_d on the vertical force for each stroke plane angle β, while fixing $\alpha_u=150°$ for $\beta=30°$ and 60°, $\alpha_u=180°$ for $\beta=90°$ (rowing ; Fig. 1(b)), and $\alpha_u=180°-\alpha_d$ for $\beta=0°$ (normal hovering ; Fig. 1(a)).

Figure 8 shows the variations of the time-averaged lift, drag and vertical force coefficients during the downstroke motion with respect to α_d

for $\beta=60°$, together with the vertical force averaged over one flapping period ($\overline{C}_V$). The behavior of the force variation at $Re=150$ is similar to that at $Re=1000$. The drag increases almost linearly with increasing α_d, but the lift is maximum near $\alpha_d=45°$ and decreases with further increase of α_d. Therefore, the vertical force during downstroke becomes maximum at $\alpha_d=75°\sim80°$ for $\beta=60°$, because $(C_V)_{down}=(C_D)_{down}\sin\beta+(C_L)_{down}\cos\beta$. The vertical force averaged over one flapping period, $\overline{C}_V$, is also maximum at $\alpha_d=75°\sim80°$ for $\beta=60°$.

Figure 9(a) shows the variation of the optimal α_d ($\tilde{\alpha}_d$) for maximum vertical force with respect to β for both Reynolds numbers. It is interesting to note that $\tilde{\alpha}_d$ is almost linearly proportional to β, indicating that the drag component is the major source of the vertical force with increasing β, whereas the lift component becomes the main source as β approaches zero. In Fig. 9(b), the maximum time-averaged vertical force coefficient (i.e. $\overline{C}_V$ at $\tilde{\alpha}_d$) is shown with respect to β. As shown, the vertical force is maximum at $\beta=60°$ for both Reynolds numbers and minimum at $\beta=90°$, which partially explains why the dragonfly hovers at $\beta=60°$ (Norberg, 1975) or less

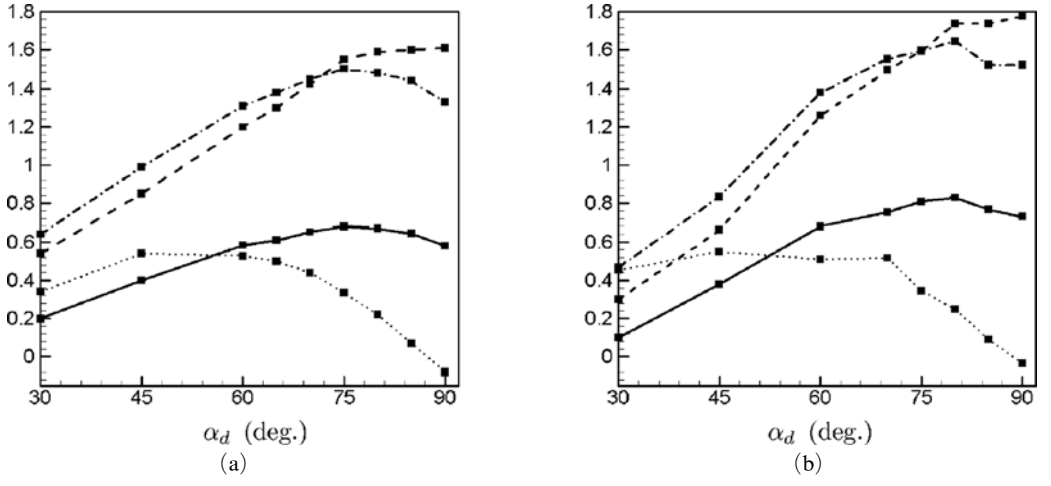

Fig. 8 (a) Variations of the time-averaged force coefficients during the downstroke motion with respect to α_d for $\beta=60°$: (a) $Re=150$; (b) $Re=1000$. ----, $(\overline{C}_D)_{down}$; ·····, $(\overline{C}_L)_{down}$; -·-·-·-, $(\overline{C}_V)_{down}$; ——, $\overline{C}_V$

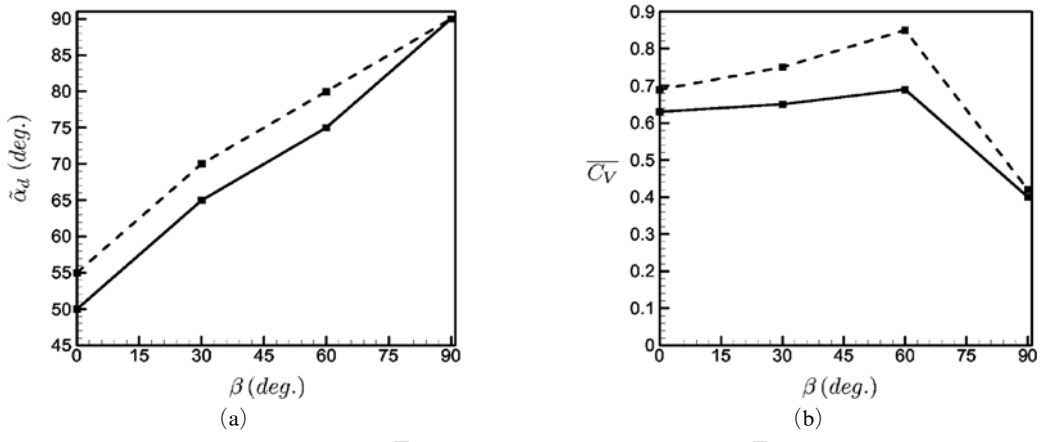

Fig. 9 Variations of the optimal α_d and $\overline{C}_V$ with respect to β: (a) $\tilde{\alpha}_d$; (b) $\overline{C}_V$ at $\tilde{\alpha}_d$. ——, $Re=150$; ----, $Re=1000$

(Wakeling and Ellington, 1997) at the Reynolds number of about 1000.

In order to analyze this interesting result, the time histories of the vertical force coefficient for $\beta=0°$, 60° and 90° are shown in Fig. 10. In the case of normal hovering ($\beta=0°$), the vertical force is generated purely by the lift component and is positive during most of flapping motion. Note also that C_V during $0\leq t/T<0.5$ is not the same as that during $0.5\leq t/T<1$ due to the vortical interaction of the wing. This asymmetry occurs even after long-time computation and is determined by the initial movement direction of the normal hovering. On the other hand, in the case of rowing ($\beta=90°$), very large positive and negative instantaneous vertical forces (as compared to those in normal hovering) exist during the flapping motion. However, due to the negative one generated during upstroke and the end of downstroke, the mean vertical force becomes smaller than that in normal hovering (see Fig. 9(b)). In the case of inclined stroke at $\beta=60°$, the negative region of the vertical force is significantly reduced as compared to that in rowing ($\beta=90°$), while keeping the large positive region of C_V. Moreover, during the early stage of upstroke, the negative vertical force is even smaller than that of the quasi-steady force (see Fig. 7(a)). Hence, the largest mean vertical force is obtained for $\beta=60°$ (Fig. 9(b)). As mentioned previously, the behavior of the vertical force during the stroke reversal cannot be explained by the delayed stall mechanism, and is associated with the interaction between the wing and the vortices, which is discussed in the following section.

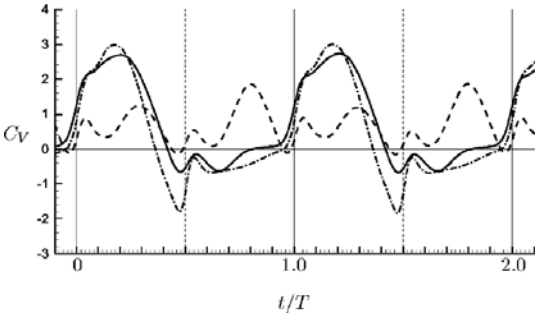

Fig. 10 Time histories of the vertical force coefficient ($Re=150$): ----, $\beta=0°$ ($\alpha_d=45°$ and $\alpha_u=135°$); -·-·-·-, $\beta=90°$ ($\alpha_d=90°$ and $\alpha_u=180°$); ——, $\beta=60°$ ($\alpha_d=75°$ and $\alpha_u=150°$)

3.2 Wing-wake interaction

Dickinson et al.(1999) suggested wing-wake interaction mechanism (called 'wake capture') for normal hovering motion during the stroke reversal. In the present study, we further elaborate on this mechanism from the time sequence of vortical motion and its interaction with the wing for an inclined stroke.

Figure 11 shows the time sequence of the spanwise vorticity for $\beta=90°$ at $Re=150$ and the instantaneous pressure at $t/T=0.45$. The wing generates a pair of vortices at the wing edges during downstroke (Figs. 11(a) and 11(b)). These vortices also move downward due to the self-induced motion. Near the end of downstroke, the wing speed is significantly reduced but the vortices keep moving downward (Fig. 11(c)). The downward velocity induced by the pair vortices impacts on the upper wing surface, which causes a high pressure region there (Fig. 11(f)) and thus generates a large negative vertical force (Fig. 7(b)) even though the wing is still moving downward. Furthermore, during the initial period of upstroke (Figs. 11(d) and 11(e)), the wing passes through the region of downward velocity induced by the pair vortices shed during the downstroke motion of the wing, which again produces a large negative vertical force on the wing (Fig. 7(b)). Therefore, in the case of rowing, the wing suffers from the vortices generated during the downstroke motion and has a relatively small value of the mean vertical force even though rowing produces a large positive vertical force during downstroke.

On the other hand, in the case of inclined stroke at $\beta=60°$, the interaction between the wing and vortices is very different from that in the case of rowing. Fig. 12 shows the time sequence of the spanwise vorticity for $\beta=60°$ at $Re=150$ and the instantaneous pressure at $t/T=0.55$. Similar pair vortices as observed in the case of rowing are generated from the leading and trailing edges of the wing during downstroke (Figs. 12(a) and 12(b)).

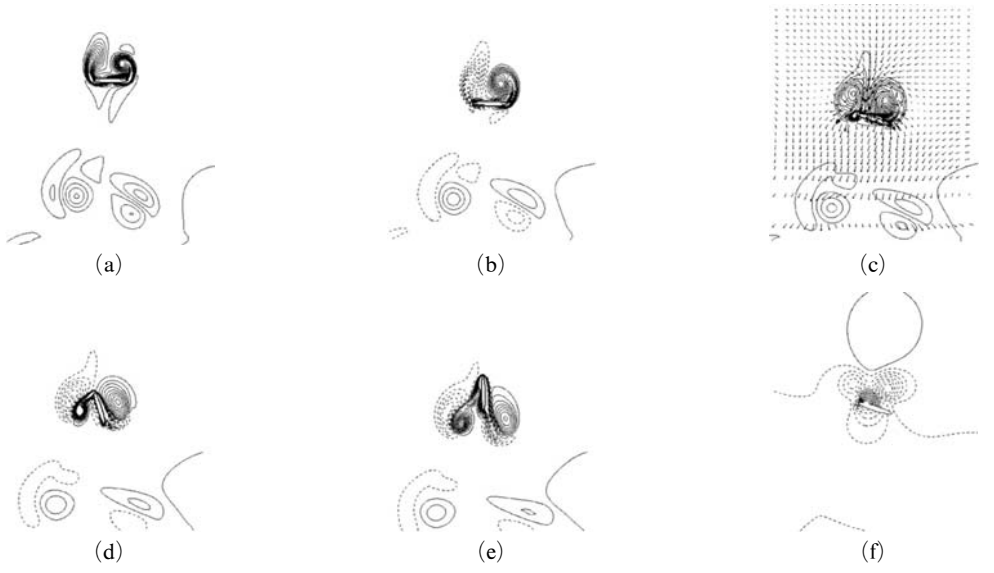

Fig. 11 Time sequence of the spanwise vorticity for $\beta=90°$ (rowing) at $Re=150$ and instantaneous pressure at $t/T=0.45$: (a) vorticity contours at $t/T=0.25$; (b) 0.35 ; (c) 0.45 ; (d) 0.55 ; (e) 0.65 ; (f) pressure contours at $t/T=0.45$. The velocity vectors are also shown in (c). The vorticity contour levels are $w_z c/u_{\max}=-10\sim10$ by increments of 0.67 and the pressure contour levels are $p/\rho u_{\max}^2=-1\sim1$ by increments of 0.067. Negative values are dashed in this figure. See Fig. 7(b) for the corresponding vertical force on the wing

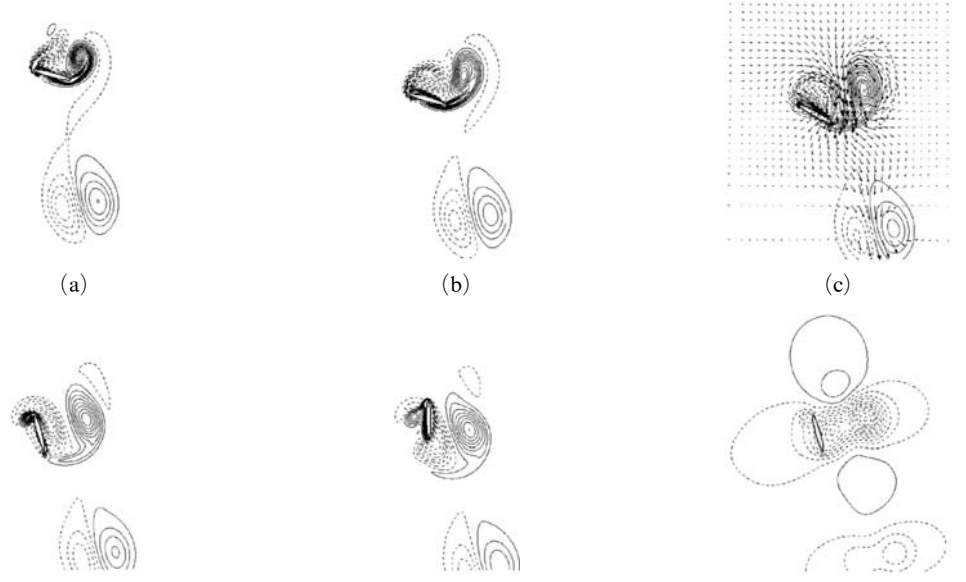

Fig. 12 Time sequence of the spanwise vorticity for $\beta=60°$ (inclined stroke) at $Re=150$ and instantaneous pressure at $t/T=0.55$: (a) vorticity contours at $t/T=0.25$; (b) 0.35 ; (c) 0.45 ; (d) 0.55 ; (e) 0.65 ; (f) pressure contours at $t/T=0.55$. The velocity vectors are also shown in (c). The vorticity contour levels are $w_z c/u_{\max}=-10\sim10$ by increments of 0.67 and the pressure contour levels are $p/\rho u_{\max}^2=-1\sim1$ by increments of 0.067. Negative values are dashed in this figure. See Fig. 7(a) for the corresponding vertical force on the wing

However, these vortices do not follow the wing trajectory but move rather in the direction of gravity. Thus, the wing is less exposed to the downwash motion induced by these vortices near the end of downstroke (Fig. 12(c)) and a much smaller negative vertical force occurs in the case of inclined stroke (Fig. 7(a)). Moreover, during the early stage of upstroke (Figs. 12(d) and 12(e)), the upper wing surface seizes the leading edge vortex shed previously during downstroke. This vortex capture results in a low pressure region on the upper wing surface during upstroke (Fig. 12(f); otherwise high pressure forms there) and a smaller negative vertical force occurs during upstroke (Fig. 7(a)). As mentioned, this kind of wing-wake interaction does not occur for $\beta=90°$, which explains the sharp decrease in the mean vertical force at $\beta=90°$ (Fig. 9(b)).

In order to see the Reynolds number effect, numerical simulations are conducted at $Re=15$ and 1000 for $\beta=60°$. Fig. 13 shows the temporal variations of the vertical force coefficient for three different Reynolds numbers. The behaviors of the vertical force are different among themselves, especially during upstroke. At $Re=15$, there is no vortex shedding because of too low Reynolds number (Fig. 14(a)) and thus one cannot expect any wing-wake interaction mechanism. Therefore, a very large negative vertical force exists during upstroke. On the other hand, the strength of shed vortices becomes higher at $Re=1000$ as shown in Fig. 14(c) and a smaller negative vertical force occurs due to the wing-wake interaction. Therefore, the effect of wing-wake interaction increases with the Reynolds number.

As mentioned earlier, the major disadvantage of an inclined stroke is the negative vertical force produced during upstroke. However, the wing-wake interaction reduces this negative vertical force and enables the hovering motion with an inclined stroke to generate a sufficient vertical force.

3.3 Rotational circulation

Dickinson et al.(1999) argued that the wing rotation near the end of stroke enhances lift because it generates a circulation on the wing. This

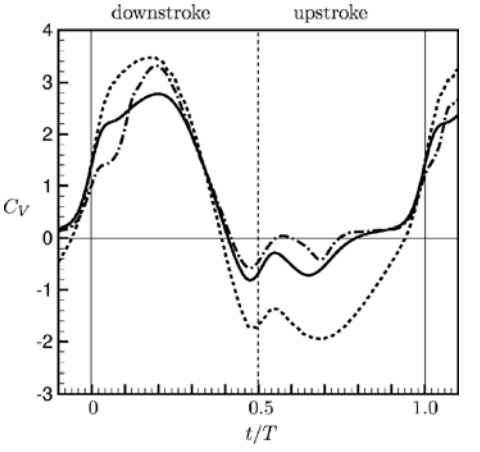

Fig. 13 Time histories of the vertical force coefficient at $\beta=60°$: ----, $Re=15$; ——, $Re=150$; -·-·-·-, $Re=1000$

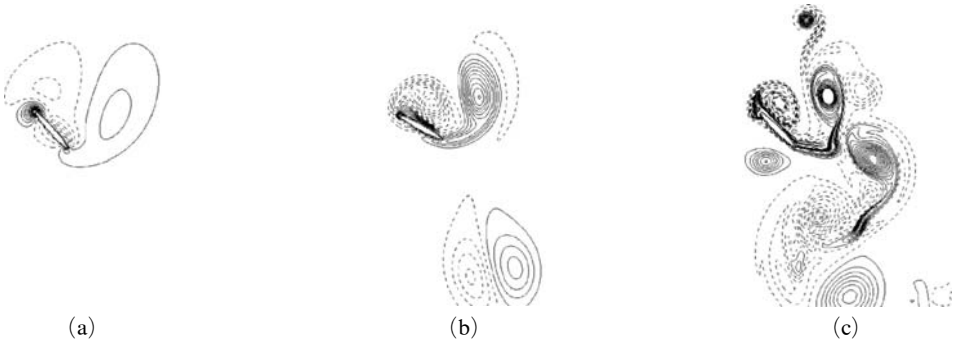

(a) (b) (c)

Fig. 14 Contours of the instantaneous spanwise vorticity for $\beta=60°$ at $t/T\simeq0.45$: (a) $Re=15$; (b) $Re=150$; (c) $Re=1000$. The contour levels are $w_z c/u_{\max}=-10\sim10$ by increments of 0.67. Negative values are dashed in this figure

argument is consistent with the result of Bennett (1970), who found that the lift force is augmented when the angle of attack increases before the stroke reversal. For a two-dimensional wing rotating with an angular velocity Ω in an inviscid fluid, the rotational circulation Γ_r can be derived theoretically, satisfying the Kutta condition (Ellington, 1984c):

$$\Gamma_r = \pi \Omega c^2 \left(\frac{3}{4} - \frac{x_0}{c} \right) \tag{16}$$

where x_0 is the distance between the axis of rotation and the leading edge. Thus, by applying the Kutta-Jukowski theorem, the hydrodynamic lift force in the vertical direction due to wing rotation is obtained:

$$F_{rot} = \rho u_d \Gamma_r \tag{17}$$

Using this theoretical estimation, we study the contribution of wing rotation to the vertical force by changing the timing of rotation. In contrast to normal hovering, however, early rotation near the end of upstroke causes a detrimental effect on the vertical force in the case of inclined stroke because drag (and thus negative vertical force) increases at the pronation. Hence, in this study, we change only the timing of supination by altering t_s (see Eq. (2) and Fig. 3). When we changed $t_s=0$ into $t_s=-0.07T$, we found that $\delta=2$ produced non-smooth $d\alpha/dt$ in time. So, we changed $\delta=2$ into $\delta=3$ for $t_s=-0.07T$, which provided smooth $d\alpha/dt$ in time with the rotation period of 20% out of the total flapping period.

Figures 15(a) and 15(b) show the time histories of the vertical force coefficients for $t_s=0$ and $-0.07T$, respectively. Note that with early rotation (Fig. 15(b)), the vertical force (C_V) is significantly reduced at the supination. Also shown in Fig. 15, the rotational hydrodynamic force is induced by wing rotation from Eq. (16). For $t_s=0$ (Fig. 15(a)), the rotational hydrodynamic force at the supination is quite small since the translational velocity of the wing is low when the wing begins to rotate. Moreover, an equal amount of negative rotational force is generated after $t/T=0.5$ because the direction of velocity is reversed. However, for $t_s=-0.07T$, a large positive rotational hydrodynamic force is generated at the supination (Fig. 15(b)). Thus, the negative vertical force is significantly reduced when rotation occurs earlier at the end of downstroke, and this is explained by the circulation theorem.

3.4 Effect of wing shape

So far, the cross-section of the wing has been taken to be an ellipse with a thickness-to-chord ratio of $h/c=0.125$ following Wang (2000). The shape of the dragonfly's wing, however, is close to a thin flat plate rather than an ellipse. Hence, in

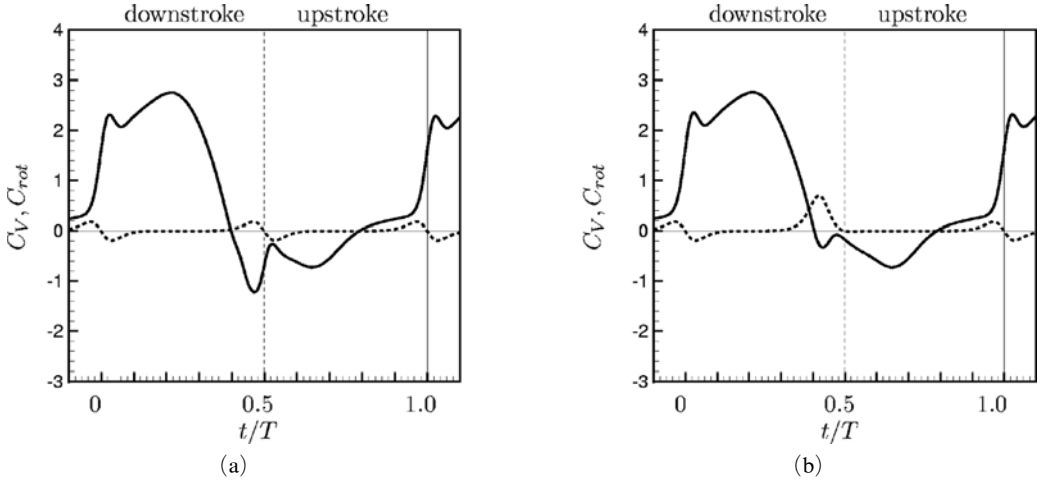

Fig. 15 Time histories of the vertical force coefficients at $\beta=60°$, $\delta=3$ and $Re=150$: (a) $t_s=0$; (b) $t_s=-0.07T$. ——, C_V; ----, C_{rot} $(=F_{rot}/\frac{1}{2}\rho u_{\max}^2 cl)$

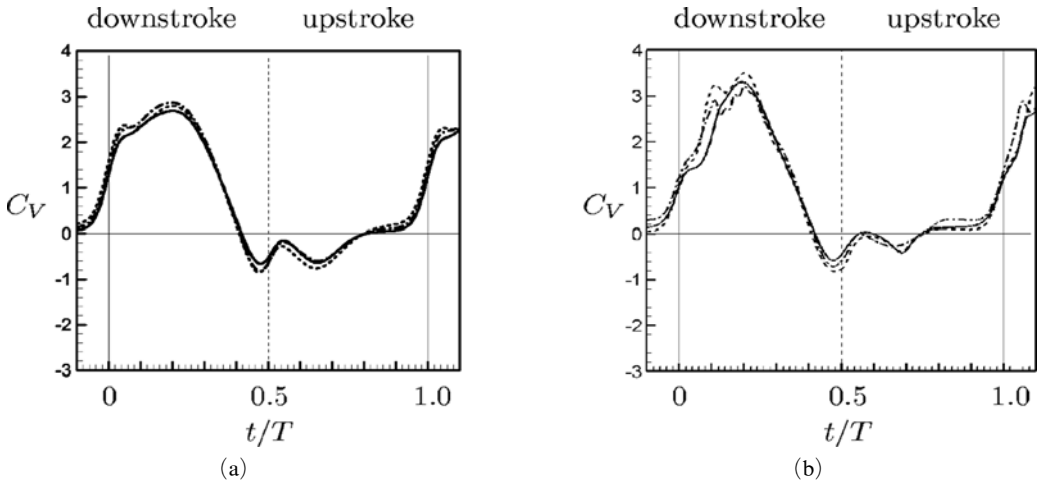

Fig. 16 Time histories of the vertical force coefficient for $\beta=60°$: (a) $Re=150$; (b) $Re=1000$. ——, Elliptic wing ($h/c=0.125$); ----, flat plate ($h/c=0.1$); -·-·-·-, flat plate ($h/c=0.05$)

order to see the effect of the wing shape on the vertical force, we conduct numerical simulations for the flat-plate wing with two different thickness-to-chord ratios of 0.1 and 0.05.

Figure 16 shows the temporal variations of the vertical force coefficient for three different wing shapes at $Re=150$ and 1000. It is clear from this figure that the behaviors of the vertical force are almost same for different wing shapes at this low Reynolds number range. Therefore, the details of the wing cross-section may not be so important in the insect flight at this Reynolds number range once it is thin enough.

4. Conclusions and Further Remarks

In this study, we simulated the hovering motion of single flapping wing using an immersed boundary method in a non-inertial reference frame, in order to investigate the mechanisms, originally conjectured by Dickinson et al.(1999), responsible for the high vertical force generated by an inclined stroke in hovering motion. Numerical simulations were performed at $Re=150$ and 1000 for different stroke plane angles and angles of attack.

We showed that an inclined stroke in hovering motion generates a high vertical force by three different mechanisms. First, during the translation period of downstroke, the vertical force is larger than that from the quasi-steady analysis due to the delayed stall mechanism. Since the attack angle is directly connected with the delayed stall, we found that the optimal angle of attack of producing maximum vertical force is a linear function of the stroke plane angle. Two other mechanisms (wing-wake interaction and rotational circulation) explain the vertical force behavior occuring during the stroke reversal, i.e., when the wing rotates and changes its direction. The mechanism of wing-wake interaction is found to be the vortex escape and capture during the stroke reversal. That is, at the end of downstroke, the wing escapes from the downwash motion induced by a pair of vortices generated during downstroke and thus a much smaller negative vertical force occurs on the wing. On the other hand, during the early stage of upstroke, the wing captures the leading edge vortex, shed previously during downstroke, on its upper surface, resulting in a low pressure region on the upper wing surface and thus a smaller negative vertical force on the wing. We also showed that the effect of wing-wake interaction is more pronounced at higher Reynolds number. Finally, the mechanism of rotational circulation is confirmed by advancing the timing of wing rotation at supination. That is, when the wing

rotates earlier near the end of downstroke, the negative vertical force is significantly reduced, and this phenomenon is also explained by the inviscid potential theory.

So far, we have considered the two-dimensional mechanisms responsible for the high vertical force generated by an inclined stroke in hovering motion. Although these two-dimensional mechanisms are crucial to high lift generation as also supported by other researchers (Wang, 2000; Wang et al., 2004), the fluid flow around insect flight is essentially three-dimensional and thus three-dimensional effects such as the spanwise helical flow found by Ellington et al.(1996) and the wing tip vortex should be considered for the explanation of high vertical force generation. These three-dimensional effects may influence the two-dimensional mechanisms investigated in the present study: e.g., the spanwise helical flow enhances the delayed stall mechanism as suggested by Ellington et al.(1996) and confirmed numerically by Liu et al.(1998), and the wing tip vortex may affect the wing-wake interaction mechanism. However, one of the most important questions is how much these three-dimensional effects contribute to the total vertical force. In order to answer this question, we currently conduct numerical simulations of flow generated by a three-dimensional flapping motion, and the result will be published elsewhere.

Acknowledgments

This work is supported by the NRL Program of the Korean Ministry of Science and Technology.

References

Beddhu, M., Taylor, L. K. and Whitfield, D., 1996, "Strong Conservative Form of the Incompressible Navier-Stokes Equations in a Rotating Frame with a Solution Procedure," *J. Comput. Phys.*, Vol. 128, pp. 427～437.

Bennett, L., 1970, "Insect Flight : Lift and Rate Change of Incidence," *Science*, Vol. 167, pp. 177～179.

Birch, J. M. and Dickinson, M. H, 2001, "Spanwise Flow and the Attachment of the Leading-Edge Vortex on Insect Wings," *Nature*, Vol. 412, pp. 729～733.

Dickinson, M. H., Lehmann, F. O. and Sane, S. P., 1999, "Wing Rotation and the Aerodynamic Basis of Insect Flight," *Science*, Vol. 284, pp. 1954～1961.

Ellington, C. P., 1984a, "The Aerodynamics of Hovering Insect Flight. I. The Quasi-Steady Analysis," *Phil. Trans. R. Soc. Lond. B*, Vol. 305, pp. 1～15.

Ellington, C. P., 1984b, "The Aerodynamics of Hovering Insect Flight. III. Kinematics," *Phil. Trans. R. Soc. Lond. B*, Vol. 305, pp. 41～78.

Ellington, C. P., 1984c, "The Aerodynamics of Hovering Insect Flight. IV. Aerodynamic Mechanisms," *Phil. Trans. R. Soc. Lond. B*, Vol. 305, pp. 79～113.

Ellington, C. P., Berg, C. van den, Willmott, A. P. and Thomas A. L. R., 1996, "Leading-Edge Vortices in Insect Flight," *Nature*, Vol. 384, pp. 626～630.

Francis, R. H. and Cohen, J., 1933, "The Flow Near a Wing Which Starts Suddenly from Rest and Then Stalls," *Rep. Memo. Aeronaut. Res. Comm.*, Vol. 1561.

Kim, D. and Choi, H., 2006, "Immersed Boundary Method for Flow Around an Arbitrarily Moving Body," *J. Comput. Phys.*, Vol. 212, pp. 662～680.

Kim, J., Kim, D. and Choi, H., 2001, "An Immersed-Boundary Finite-Volume Method for Simulations of Flow in Complex Geometries," *J. Comput. Phys.*, Vol. 171, pp. 131～150.

Liu, H., Ellington, C. P., Kawachi, K., Berg, C. and Willmott, A. P., 1998, "A Computational Fluid Dynamic Study of Hawkmoth Hovering," *J. Exp. Biol.*, Vol. 201, pp. 461～477.

Newman, J. N., 1986, *Marine Hydrodynamics.*, The MIT Press.

Norberg, R. A., 1975, "Hovering Flight of the Dragonfly Aeschnia Juncea L., Kinematics and Aerodynamics," *In Swimming and Flying in Nature.*, Prenum Press, Vol. 2, pp. 763～781.

Pauley, L. P., Moin, P. and Reynolds, W. C., 1990, "The Structure of Two-Dimensional Separation," *J. Fluid Mech.*, Vol. 220, pp. 397～411.

Sun, M. and Tang, J., 2002, "Unsteady Aerodynamic Force Generation by a Model Fruit Fly Wing in Flapping Motion," *J. Exp. Biol.*, Vol. 205, pp. 55～70.

Vogel, S., 1994, *Life in Moving Fluids.*, Princeton University.

Wakeling, J. M. and Ellington, C. P., 1997, "Dragonfly Flight II. Velocities, Accelerations and Kinematics of Flapping Flight," *J. Exp. Bio.*, Vol. 200, pp. 557～582.

Walker, P. B., 1931, "Experiments on the Growth of Circulation About a Wing and an Apparatus for Measuring Fluid Motion," *Rep. Memo. Aeronaut. Res.*, No. 1402.

Wang, Z. J., 2000, "Two Dimensional Mechanism for Insect Hovering," *Phys. Rev. Lett.*, Vol. 85, pp. 2216～2219.

Wang, Z. J., Birch, J. M. and Dickinson, M. H., 2004, "Unsteady Forces and Flows in Low Reynolds Number Hovering Flight: Two-Dimensional Computations vs Robotic Wing Experiments," *J. Exp. Biol.*, Vol. 207, pp. 449～460.

Weis-Fogh, T. and Jenson, M., 1956, "Biology and Physics of Locust Flight," *Philos. T. Roy. Soc. London B*, Vol. 239, pp. 415～584.